Computer-generated mesoporous materials and associated structural characterization

Tiphaine Galy[a],[1], Du Mu[b],[1], Michal Marszewski[a], Laurent Pilon[a],[*]

[a] Mechanical and Aerospace Engineering Department, Henry Samueli School of Engineering and Applied Science, University of California, Los Angeles, United States
[b] MOE Key Laboratory of Thermo-Fluid Science and Engineering, School of Energy and Power Engineering, Xi'an Jiaotong University, Xi'an 710049, PR China

ARTICLE INFO

ABSTRACT

This study aims to computationally generate and fully characterize realistic three-dimensional mesoporous materials. Notably, a new algorithm reproducing gas adsorption porosimetry was developed to calculate the specific surface area and pore size distribution of computer-generated structures. The diffusion-limited cluster-cluster aggregation (DLCCA) method was used to generate point-contact or surface-contact mesoporous structures made of monodisperse or polydisperse spherical particles. The generated structures were characterized in terms of particle overlapping distance, porosity, specific surface area, interfacial area concentration, pore size distribution, and average pore diameter. The different structures generated featured particle radius ranging from 2.5 to 40 nm, porosity between 35 and 95%, specific surface area varying from 35 to 550 m^2/g, and average pore diameter between 3.5 and 125 nm. The specific surface area and pore size distribution of computer-generated mesoporous materials were in good agreement with experimental data reported for silica aerogels. Finally, widening the particle size distribution and increasing the particle overlapping were shown to strongly decrease the specific surface area and increase the average pore size of the mesoporous structures. The developed computational tools and methods can accelerate the discovery and optimization of mesoporous materials for a wide range of applications.

1. Introduction

Mesoporous materials, such as aerogels, feature pore size ranging from 2 to 50 nm [1], large specific surface area (100–1200 m^2/g) [2–6] and a wide range of porosity (30–99%) [2,3,7]. Given all their attractive attributes, aerogels featuring various material composition and high porosity (80–99%) have been considered for a wide range of applications including adsorbents [4,8], catalysts [4–6], low-k dielectric materials [9], and thermal insulation for building and aerospace applications [3,5,10,11]. The thermophysical properties of mesoporous materials have been shown to strongly depend on their nanoscale architecture. For example, increasing the porosity of silica aerogels reduces their dielectric constant [9], strength [12], and thermal conductivity [7]. In addition, smaller pores lead to smaller thermal conductivity [10] and higher optical transparency [13] while larger pores lead to better permeability [8]. Furthermore, contact or coalescence between adjacent SiO_2 nanoparticles reinforces the strength of the aerogel [14] and has been shown experimentally to affect their structure [15].

Experimental optimization of mesoporous materials by trial and error to achieve the desired thermophysical properties can be challenging and time consuming. Alternatively, computer simulations can quickly generate various representative mesoporous structures with a wide range of structural parameters such as porosity, specific surface area, and pore size distribution [16–21]. Then, nanostructure-property relationship can be derived and used to identify the optimum nanostructure for the desired properties [18,20,21].

This study aims to numerically generate and characterize a wide variety of three-dimensional mesoporous structures featuring aggregated spherical nanoparticles with either point-contact or surface-contact. The generated porous structures were fully characterized in terms of porosity, specific surface area, average pore size, and pore size distribution, in complete analogy with experimental gas adsorption porosimetry. Most notably, a new algorithm was developed to compute the specific surface area and pore size distribution of the computer-generated mesoporous structures. Whenever possible, the results were compared with experimental data reported in the literature.

* Corresponding author at: Engineering IV, 420 Westwood Plaza, Los Angeles, CA 90095-1597, United States.
 E-mail address: pilon@seas.ucla.edu (L. Pilon).
 [1] These authors contributed equally.

Nomenclature

A_g	specific surface area, m^2/g
A_i	interfacial area concentration, m^{-1}
C_{N_2}	cross-sectional area of a nitrogen molecule, m^2
d	interparticle distance, nm
$\bar{d}$	average interparticle distance, nm
$\bar{d}^*$	dimensionless average interparticle distance, $\bar{d}^* = \bar{d}/2r_s$
$\bar{d}_i$	average diameter of empty space in pores, nm
d_p	pore diameter, nm
$\bar{d}_p$	average pore diameter, nm
f_v	particle volume fraction
L	dimension of the cubic simulation domain, nm
l_o	overlapping distance, nm
$\bar{l}_o^*$	dimensionless average overlapping distance, $\bar{l}_o^* = \bar{l}_o/2r_s$
l_s	traveling distance of particles during structure generation, nm
N_A	Avogadro constant, $N_A = 6.02 \times 10^{23}$ mol^{-1}
	number of elementary cubes in simulation domain
N_m	monolayer capacity, mol/g
N_s	number of spheres in an aggregate
N_t	initial number of spheres for aggregate generation
n_c	final number of clusters
r_s	particle radius, nm
$\bar{r}_s$	mean radius of polydisperse particles, nm

S_i	apparent surface area at iteration i, m^2
S_0	total surface area, m^2
t_i	"adsorbate" layer thickness at iteration i, nm
V_i	apparent pore volume at iteration i, m^3
V_p	pore volume, m^3
$V_{p,cu}$	cumulative pore volume, m^3
$V_{p,tot}$	total pore volume, m^3
v_p	specific pore volume, m^3/g

Greek symbols

Δt	change in adsorption layer thickness, nm
Δx	cube size, nm
ϕ	porosity
ρ_{eff}	effective density of the mesoporous silica, g/m^3
ρ_s	silica density, $\rho_s = 2.2$ g/m^3
σ_s	standard deviation of a particle radius distribution, nm

Superscripts and subscripts

|	
BET	refers to the Brunauer-Emmett-Teller (BET) method
PC	refers to point-contact structure
PSD	refers to the pore size distribution algorithm
SC	refers to surface-contact structure

2. Background

2.1. Aerogels, ambigels, and xerogels

Synthesis of aerogels can be divided into four successive stages namely (1) sol phase, (2) gelation, (3) aging, and (4) drying [2]. During the sol phase, the gel precursor reacts and forms nanoparticles. The gelation occurs when the nanoparticles start aggregating and forming a network. Nanoparticles clusters form and grow by aggregation of individual particles and by collision with other clusters. The process progressively leads to a continuous network [22]. Aging results in the growth of necks between particles which strengthens the network [23]. During drying, the solvent contained in the pores is removed. The drying method strongly affects the porosity and pore size distribution of the final mesoporous structure [22,24]. The capillary pressure imposed by the solvent on the network during drying results in shrinkage of the gel structure. Gels dried quickly in the open air have typical porosity less than 50% due to significant shrinkage and are referred to as xerogels [25]. By contrast, aerogels reach porosity above 80% thanks to supercritical CO$_2$ drying at high pressure so as to minimize capillary

forces. Alternatively, capillary forces can also be minimized by exchanging the pore liquid with a non-polar solvent featuring low surface tension (e.g., hexane or cyclohexane) and by slow drying at ambient temperature and pressure [25]. Gels dried via non-polar solvent exchange at ambient temperature and pressure are referred to as ambigels [24]. Aerogels have larger porosity and pore size than ambigels and xerogels [22] while ambigels typically feature porosity and pore size between those of xerogels and aerogels [24]. Finally, Fig. 1 shows scanning (SEM) and transmission (TEM) electron microscopy images of typical silica aerogels [13,26,27]. It indicates that actual silica aerogels consist of distinct overlapping nanoparticles.

2.2. Numerically-generated mesoporous structures

Several particle aggregation models have been developed to numerically simulate the gelation process [28]. They differ mainly in the way the particle clusters grow and diffuse. For example, the monomer-cluster aggregation method consists of clusters formed from particles added one-by-one throughout the process [28]. Alternatively, the cluster-cluster aggregation method consists of a given initial number of
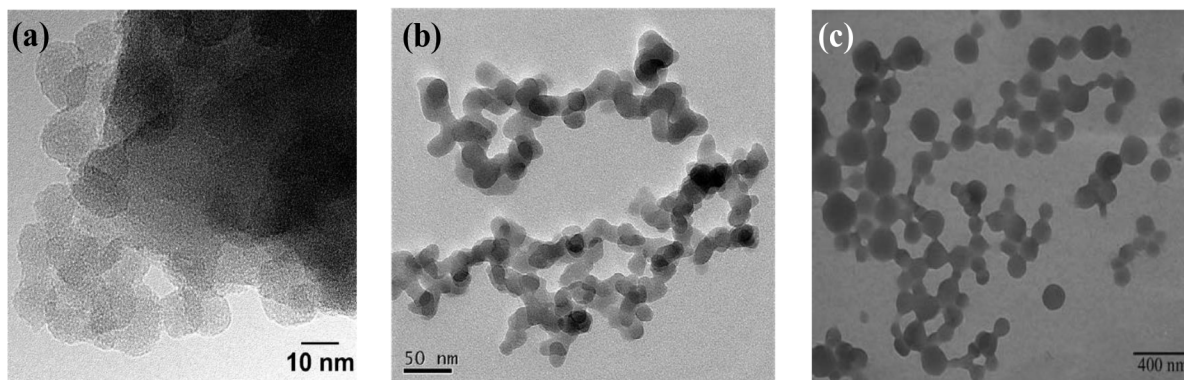
Fig. 1. TEM images of (a), (b) silica aerogels (reprinted with permission from Ref. [13] and Ref. [26] Copyright Springer International Publishing A.G. 2007 and Copyright Elsevier B.V. 2013, respectively), and (c) silica solution during gelation (reprinted with permission from Ref. [27] Copyright Springer International Publishing A.G. 2007).

particles moving, colliding, and forming clusters which themselves diffuse, collide, and grow [22]. The cluster-cluster aggregation method generates less compact structures (i.e., with lower fractal dimension) than the monomer-cluster method and has been reported to be more representative of the aerogel gelation process [22].

Moreover, one can distinguish diffusion-limited aggregation from reaction-limited aggregation [22]. Under diffusion-limited aggregation, the colliding clusters aggregate immediately and irreversibly upon contact [22]. By contrast, under reaction-limited aggregation, particles or clusters can collide several times before aggregating and the connection between clusters is reversible, i.e., clusters can break apart [22]. Reaction-limited aggregation is more representative of the gelation process of structures in which chemical bonds are formed after several collisions [22]. On the other hand, diffusion-limited aggregation corresponds better to the gelation of reactive specimens forming bonds after few collisions [22,29]. For example, for silica aerogel synthesis, the occurrence of bonds formation depends on the pH and solution composition [15]. At high pH, silica is very reactive and nanoparticles form bonds only after few collisions [29]. Finally, the diffusion-limited cluster-cluster aggregation (DLCCA) method has been shown to reproduce the gelation growth process and the cluster size distribution of gels [22,29,30].

2.3. Numerically-generated silica aerogels

Silica aerogels have been generated numerically as fractal structures using aggregation models to predict their morphology [16,17,19], physical characteristics [18,21], and thermophysical properties [31–33]. Numerically-generated silica aerogels by DLCCA method have considered point-contact structures [21,31–33] and surface-contact structures with overlapping particles [18,19]. For example, Primera et al. [17] numerically generated 3D silica aerogel structures by the DLCCA method. The generated structures consisted either of monodisperse cubic particles less than 4 nm in size or of bimodal mixture of cubic particles of size $r_{s_1} \leqslant 4$ nm and $r_{s_2} = 7 r_{s_1}$ nm with porosity ranging from 80 to 95%. The authors also characterized them in terms of specific surface area, average pore size, and pore size distribution.

Morales et al. [19] developed a diffusion-limited monomer-cluster aggregation algorithm to generate surface-contact silica structures with monodisperse spherical particles. The particle radius was 1.1 or 1.2 nm and the porosity ranged from 80 to 90%. The authors showed that the mechanical strength of computer-generated surface-contact silica aerogel structures agreed well with experimental measurements [18]. Similarly, Ma et al. [21] used DLCCA method to generate mesoporous silica structures and model their elastic properties using finite element method (FEM). The structures consisted of monodisperse spherical silica particles with arbitrary diameter and porosity ranging from 92 to 99%. The authors showed that increasing the aerogel density reinforced its mechanical stiffness. They also derived a scaling relation between the elastic bulk modulus and the effective density of the DLCCA silica aerogel structures.

Lallich et al. [32] used computer-generated DLCCA aggregates with point-contact spherical monodisperse particles with radius of 3.5, 4.5, and 7.25 nm and porosity around 90% to predict the extinction coefficient and scattering albedo of silica powders. Hasmy et al. [31] used computer-generated DLCCA structures with monodisperse and polydisperse nanoparticles to characterize the X-ray scattered intensity by silica aerogels. They compared their results with experimental small-angle X-ray scattering (SAXS) measurements for structures with porosity around 95% and particle radius around 2.3 nm. They showed that the scattered X-ray intensity calculated from the DLCCA structures was in qualitative agreement with experimental measurements.

Furthermore, Zhao et al. [33] used DLCCA-generated structures with point-contact monodisperse silica nanoparticles of radius less than 2.5 nm and with porosity ranging from 85 to 98% to predict the effective thermal conductivity of silica aerogels. They used finite volume

method (FVM) to solve the combined two-flux radiative transfer equation and the energy equation through the generated structures.

Finally, pore size distribution (PSD) has been previously determined numerically either from simulated nitrogen adsorption isotherms calculated by Grand Canonical Monte Carlo (GCMC) simulations [34,35] or by a 2D triangulation method applied to 3D structures [16,17,19]. Unfortunately, the GCMC method is time consuming and computationally complex [34]. On the other hand, the 2D triangulation method calculates pore sizes from cross-sections of the pores. Unfortunately, the extension of the triangulation method to 3D pore volumes is far from trivial [36].

2.4. Experimental characterization methods

Nitrogen adsorption porosimetry is commonly used experimentally to characterize the specific surface area $A_{g,BET}$ (in m^2/g), pore size distribution (PSD), and open porosity ϕ of mesoporous materials [1,37]. The specific surface area can be obtained by the Brunauer-Emmett-Teller (BET) method based on the expression [37,38]

$$A_{g,BET} = N_m N_A C_{N_2} \tag{1}$$

where N_A is the Avogadro constant (in mol^{-1}) and C_{N_2} is the cross-sectional area of a N_2 molecule adsorbed in a monolayer (in m^2) while N_m is the measured monolayer capacity (in mol/g), defined as the number of moles of N_2 needed to cover the surface of the pores in 1 g of porous material with a monolayer of N_2.

Moreover, the Barrett-Joyner-Halenda (BJH) method [39] is usually used to obtain the pore size distribution (PSD) of mesoporous materials. The BJH method assumes that the pores are cylindrical with diameter d_p and relies on the Kelvin equation relating the pore filling pressure to the radius of curvature of the adsorbate [40]. This estimate is then corrected for the layer of adsorbate present on the pore walls, using the measured statistical film thickness curve [41]. The BJH analysis provides (i) the incremental PSDs, i.e., the volume $V_{p,i}$ of pores having diameter between d_p and $d_p + \Delta d_p$ as a function of pore diameter d_p, and (ii) the differential PSDs, i.e., $dV_{p,cu}/dd_p$ as a function of d_p, where $V_{p,cu}$ is the cumulative pore volume of pores with diameter smaller than d_p.

The open porosity ϕ can be determined from the material bulk density ρ_s (in g/cm^3) and the measured specific pore volume v_p (in m^3/g) as [1]

$$\phi = \frac{v_p}{\frac{1}{\rho_s} + v_p}. \tag{2}$$

Here, the specific pore volume v_p is the volume occupied by the pores per unit mass of mesoporous material and can be expressed as [17,22]

$$v_p = \frac{1}{\rho_{eff}} - \frac{1}{\rho_s} \tag{3}$$

where ρ_{eff} is the effective density of the mesoporous material. Note that Eqs. (2) and (3) were obtained by ignoring the mass of air contained in the pores ($\rho_{air} \ll \rho_s$). Then, the effective density ρ_{eff} can be estimated as

$$\rho_{eff} = \rho_s (1 - \phi). \tag{4}$$

Experimentally, the specific pore volume v_p is estimated from the amount of nitrogen adsorbed at relative pressure $P/P_0 = 0.95$ close to saturation, i.e., when all pores are filled with N_2, where P_0 is the saturation pressure of N_2 [1]. Then, the measured v_p is used to calculate ϕ [Eq. (2)] and ρ_{eff} [Eq. (3)]. However, note that Eqs. (3) and (4) are valid when all pores are open. Finally, the average pore diameter $\bar{d}_p$ of mesoporous materials can be estimated by treating the pores as cylindrical such that [17,42]

$$\bar{d}_p = \frac{4 v_p}{A_g}. \tag{5}$$

Overall, although point-contact structures are easier to characterize in terms of porosity, specific surface, and average pore size, the degree of overlapping among constituent particles should be considered as an important parameter in computer-generated mesoporous structures. Unfortunately, several studies considering computer-generated surface-contact structures did not quantify the effect of particle overlapping on the specific surface area and pore size distribution of the generated structures [17–19,21]. In addition, the range of porosity (80–99 %) investigated was relatively limited. This study aims to numerically generate realistic mesoporous structures similar to ambigels and aerogels using the DLCCA method for a wide range of particle radius between 2.5 and 40 nm and porosity between 35 and 95%. It also aims to characterize these structures in terms of specific surface area A_g, total porosity ϕ, average pore diameter $\bar{d}_p$, and incremental, cumulative, and differential PSDs. A new algorithm reproducing experimental gas adsorption porosimetry measurements and BJH analysis is proposed to obtain the PSD of the computer-generated mesoporous materials. Particular attention was paid to the effect of particle overlapping and polydispersity on the structural properties.

3. Analysis

3.1. Aerogel and ambigel structure generation

The DLCCA method was used to generate aerogel and ambigel structures represented as fractal aggregates of monodisperse or polydisperse nanoparticles. This method was chosen because it can reproduce the gelation growth process and the geometry of the gel structure [22,29,30], as previously discussed. The input parameters of the DLCCA method were (i) the initial number of monodisperse nanoparticles N_t, (ii) their radius r_s, (iii) the final number of clusters n_c, and (iv) the dimension L of the cubic simulation domain. The DLCCA algorithm created the structures in four steps: (1) the N_t particles were randomly dispersed in a $L \times L \times L$ cubic simulation domain. (2) Randomly selected particles or clusters were set in motion in random directions by an incremental and arbitrary traveling distance l_s until they collided with another particle or cluster. (3) If the interparticle distance d, defined as the distance between the centers of two adjacents particles, was equal or smaller than the particle diameter, the particles merged into one cluster that continued moving as a whole in subsequent iterations. (4) The above process was repeated until the number of clusters decreased to a predefined final number of clusters n_c. Periodic boundary conditions were adopted to prevent particles or clusters from exiting the simulation domain.

Two types of nanostructures with monodisperse nanoparticles were generated namely (i) point-contact structures where particles touched at a point but did not overlap and (ii) surface-contact structures consisting of overlapping spherical particles. These two types of structures were denoted by the subscript "PC" and "SC", respectively. To generate point-contact structures, the interparticle distance d was calculated after each collision. If the interparticle distance d was smaller than $2r_s$, the moving particle or cluster was stepped back in the opposite direction to a new position such that $d = 2r_s$. The distance between adjacent particles was calculated again and if two adjacent particles were still overlapping, they were removed. The fraction of particles removed over the initial number of particles N_t increased with decreasing porosity ϕ and ranged from 11 to 71% as the porosity ϕ decreased from 95 to 50%. Therefore, in point-contact structures, the final total number of particles N_s was less than the initial number of particles N_t while $N_s = N_t$ for surface-contact structures. The porosity ϕ of the final structure was varied between 35 and 95% by decreasing the number of particles N_t. The final number of clusters n_c was set to be less than 2% of the total number of particles N_t. The length L of the simulated cubic domain was set to $L = 40r_s$ to ensure that the computational domain was sufficiently large to be considered a representative elementary volume of mesoporous material. Here, the particle radius r_s ranged from 2.5 to 40 nm and N_s between 750 and 15,000.

Mesoporous structures with surface-contact consisting of polydisperse nanoparticles were also generated and characterized. To do so, the DLCCA algorithm was first used to generate surface-contact structures with monodisperse particles. Then, the radius of randomly selected particles was modified so as to follow a Gaussian distribution $f(r_s)$ given by

$$f(r_s) = \frac{1}{\sigma_s \sqrt{2\pi}} \exp\left[-\frac{(r_s - \bar{r}_s)^2}{2\sigma_s^2} \right] \tag{6}$$

where $\bar{r}_s$ is the mean particle radius (in nm), and σ_s is the associated standard deviation (in nm). The particle radius was limited to the range $\bar{r}_s - 2\sigma_s \leqslant r_s \leqslant \bar{r}_s + 2\sigma_s$. Finally, to facilitate comparison with structures consisting of monodisperse spheres, the average radius $\bar{r}_s$ was taken as 2.5, 5, and 10 nm while the standard deviation was taken as either $\sigma_s = \bar{r}_s/2.5$ or $\bar{r}_s/5$. Here, porosity ϕ varied between 60 and 95% for N_s ranging from 6900 to 800, respectively.

3.2. Structural characterization - monodisperse nanoparticles

3.2.1. Overlapping distance

Let us define the interparticle distance d in computer-generated mesoporous structures with monodisperse nanoparticles as the distance between the center of two adjacent particles. Then, the overlapping distance can be expressed as $l_o = 2r_s - d$, as illustrated in Fig. 2(a). The average interparticle distance among all overlapping particles in the aggregate is denoted by $\bar{d}$ and the dimensionless average interparticle distance can be defined as $\bar{d}^* = \bar{d}/2r_s$. For point-contact structures, d^* is such that $\bar{d}^* = \bar{d}/2r_s = 1$ while that of surface-contact structures is such that $\bar{d}^* < 1$. Similarly, the dimensionless average overlapping distance of surface-contact structures can be defined as $\bar{l}_o^* = \bar{l}_o/2r_s = 1 - \bar{d}/2r_s$ and ranged between 0 and 1. For surface-contact structures, the
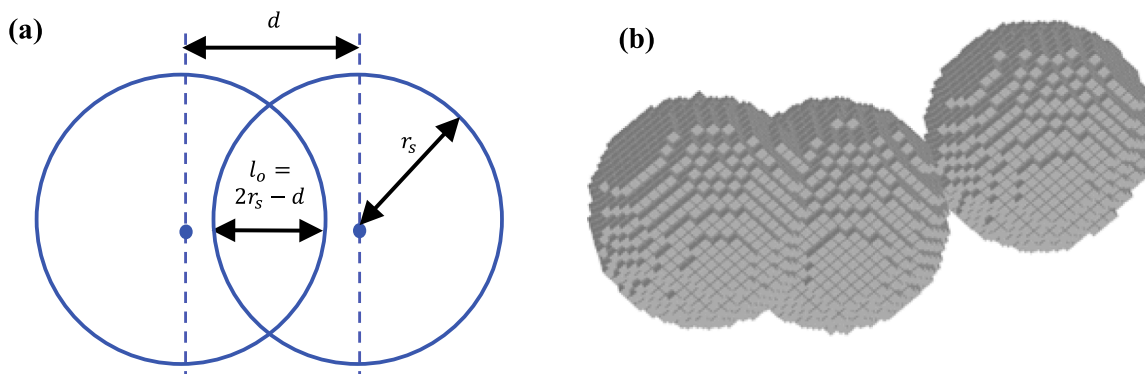
(a)

(b)

Fig. 2. (a) Illustration of the overlapping distance $l_o = 2r_s - d$ and (b) example of cube discretization of a surface-contact cluster numerically generated by DLCCA for porosity ϕ and specific surface area A_g calculations.

distance l_s traveled incrementally by particles or clusters during DLCCA structure generation may affect $\bar{d}$ and $\bar{l}_o$. Specifically, $\bar{d}$ was found to increase with decreasing l_s but remained unchanged for $l_s \leqslant r_s/2.5$ for r_s = 2.5 nm and ϕ = 50 and 95%. Thus, the traveling distance was set to $l_s = r_s/2.5$ to obtain a structure independent of the numerical parameter l_s, i.e., to achieve a numerically-converged structure. The dimensionless average overlapping distance $\bar{l}_o^*$ and the fraction of overlapping particles among the N_s particles in the structure were computed for the generated surface-contact structures. Here, the porosity ranged between 35 and 95% and the particle radius was taken as r_s = 2.5, 5, and 10 nm.

3.2.2. Porosity, specific surface area, and interfacial area concentration

For point-contact structures with monodisperse spherical particles of radius r_s, porosity ϕ, specific surface area $A_{g,PC}$ (in m^2/g), and interfacial area concentration or surface area per unit volume $A_{i,PC}$ (in m^{-1}) can be expressed as [15,22]

$$\phi = \frac{V_0}{L^3} = 1 - f_v = 1 - \frac{4\pi N_s r_s^3}{3L^3}, \quad A_{g,PC} = \frac{3}{\rho_s r_s}, \quad \text{and} \quad A_{i,PC} = A_{g,PC}\rho_s f_v.$$
(7)

Here, V_0 is the total pore volume of the structure, f_v is the volume fraction of the simulation cell occupied by the particles, and ρ_s is the density of the spherical particles. For the purpose of illustration and comparison with experimental data, ρ_s was taken as the density of bulk silica, i.e., ρ_s = 2.2 g/m^3 [15].

For surface-contact structures with monodisperse particles, f_v, ϕ, $A_{g,SC}$, and $A_{i,SC}$ were calculated numerically by discretizing the particles into small cubes of side Δx, as illustrated in Fig. 2(b). The particle volume fraction f_v was calculated by adding the volume Δx^3 of all cubes located inside the N_s particles. Note that when two adjacent particles overlapped, the cubes contained in both particles were not double-counted. Moreover, the specific surface area $A_{g,SC}$ was estimated by adding up surface areas of the cubes' faces S_{ij} located at the surface of the particles according to

$$A_{g,SC} = \frac{S_0}{\rho_s V_c} = \frac{\sum_{i=1}^{N_s}\sum_{j=1}^{6N_{c,i}} S_{ij}}{\rho_s V_c}.$$
(8)

Here, S_0 is the total internal surface area of the porous structure, $N_{c,i}$ is the number of cubes of volume Δx^3 inside particle i, V_c is the volume occupied by all cubes (i.e., $V_c = f_v L^3$), and j denotes the surfaces of cubes located in particle i. If the surface next to surface j in particle i was in contact with another cube then $S_{ij} = 0$, otherwise surface j was located at the surface of the particle i so that $S_{ij} = \Delta x^2$. Finally, the expression for interfacial area concentration $A_{i,PC}$ for point-contact structures given by Eq. (7) was also valid for surface-contact structures with either monodisperse or polydisperse particles.

The algorithm for computing particle volume fraction, porosity, and specific surface area by numerical discretization was first validated with one particle of radius r_s = 4 nm set in a cubic simulation domain of length L = 10 nm corresponding to porosity ϕ = 73.2% and specific surface area A_g = 340.9 m^2/g. The method was further validated with a structure consisting of two overlapping particles with r_s = 2 nm, L = 6 nm, and d = 2 nm corresponding to porosity ϕ = 73.8% and specific surface area A_g = 597.3 m^2/g (see Table S1 in Supporting Information). The volume fraction f_v, porosity ϕ, and specific surface area A_g were found to be independent of the discretization Δx for $\Delta x/r_s$ $\leqslant$0.04 when the results were numerically converged. In addition, the porosity ϕ and specific surface area $A_{g,PC}$ for point-contact structures generated by DLCCA method were also computed numerically with the above-described discretization method. Results for f_v and $A_{g,PC}$ calculated by numerical discretization fell within 5% of predictions by exact analytical expressions [Eq. (7)] further confirming the validity of the algorithm.

Finally, dimensionless average overlapping distance $\bar{l}_o^*$, porosity ϕ, specific surface area A_g, and interfacial area concentration A_i reported

in the present study correspond to the average of at least three computer-generated structures. The associated relative standard deviations were shown in the plots only when they were larger than the symbols. Similarly, error bars were represented for experimental data retrieved from the literature (Refs. [43–47]) whenever they were reported.

3.2.3. Pore size distributions

The pore size distribution was calculated in three steps. First, the computer-generated mesoporous structure was iteratively filled with "adsorbate" layers of thickness Δt to mimic N_2-adsorption porosimetry measurements. At each iteration i, the total volume V_i of unfilled space in the pores and the total surface area S_i of the interface between the "adsorbate" layer and the unfilled space were computed. Second, the data for the volumes $(V_i)_{0 \leqslant i \leqslant N}$ and surface areas $(S_i)_{0 \leqslant i \leqslant N}$ were analyzed with an algorithm based on the BJH method [39] to calculate the volumes $(V_{p,i})_{0 \leqslant i \leqslant N-1}$ of pores with diameter $\bar{d}_{p,i}$. Third, the incremental $V_{p,i}$, cumulative $V_{p,cu}$, and differential $dV_{p,cu}/dd_p$ pore size distributions were calculated.

The initial pore volume $V_0 = \phi L^3$ (in m^3) and interfacial surface area $S_0 = A_g \rho_s V_c$ (in m^2) of the as-generated structure (i.e., without "adsorbate") were calculated using the discretization method discussed previously. Then, at iteration $i = 1$, the particle radius was enlarged by a thickness Δt representing the thickness of a monolayer of "adsorbate". The total volume of unfilled space in the pores V_1 (in m^3) and the total surface area of the interface between the "adsorbate" layer and the unfilled space S_1 (in m^2) were calculated using the same discretization method. This procedure was repeated iteratively for $i > 1$ to yield $(V_i)_{1 \leqslant i \leqslant N}$ and $(S_i)_{1 \leqslant i \leqslant N}$ corresponding to an "adsorbate" layer thickness $t_i = i\Delta t$. After the last iteration $i = N$, all pores were filled with "adsorbate", i.e., $V_N = 0$ m^3 and $S_N = 0$ m^2.

Once the dataset for $(V_i)_{0 \leqslant i \leqslant N}$ and $(S_i)_{0 \leqslant i \leqslant N}$ was generated, it was analyzed based on the BJH method [39]. Between steps $N-1$ and N, the "adsorbate" layer thickness was increased from t_{N-1} to t_N, thus completely filling the largest pores. Therefore, the largest pores had diameter between $d_{p,N-1} = 2t_{N-1}$ and $d_{p,N} = 2t_N$ (see Fig. 3) and the average pore diameter $\bar{d}_{p,N-1}$ of the largest pores can be approximated as

$$\bar{d}_{p,N-1} = \frac{d_{p,N-1} + d_{p,N}}{2}.$$
(9)

The volume V_{N-1} and surface area S_{N-1} corresponded to the total volume and surface area of the unfilled space in the largest pores, i.e., the pores with diameter between $d_{p,N-1}$ and $d_{p,N}$. Assuming that this unfilled space in the largest pores at iteration $N-1$ had cylindrical geometry, its average diameter $\bar{d}_{N-1}$ can be expressed as

$$\bar{d}_{N-1} = \frac{4V_{N-1}}{S_{N-1}}.$$
(10)

Then, from geometric considerations (see Fig. 3), the volume $V_{p,N-1}$ and the surface area $S_{p,N-1}$ of the largest pores with average pore diameter $\bar{d}_{p,N-1}$ can be related to the dimensions of the unfilled space according to

$$\frac{V_{p,N-1}}{V_{N-1}} = \left(\frac{\bar{d}_{p,N-1}}{\bar{d}_{N-1}}\right)^2 \quad \text{and} \quad \frac{S_{p,N-1}}{S_{N-1}} = \frac{\bar{d}_{p,N-1}}{\bar{d}_{N-1}}.$$
(11)

Subsequent volume $V_{p,i}$ and surface area $S_{p,i}$ of smaller pores filled between iterations i and $i + 1$ were calculated using the same method. However, the unfilled space volume V_i and surface area S_i at iteration i had to be corrected for the contribution of larger pores whose average diameter $\bar{d}_{p,i+1}$ has already been estimated, as illustrated in Fig. 3. Specifically, the volume V_i was corrected for the volume of unfilled space in pores contained in the pores with diameter larger than $d_{p,i+1}$ already accounted for to yield
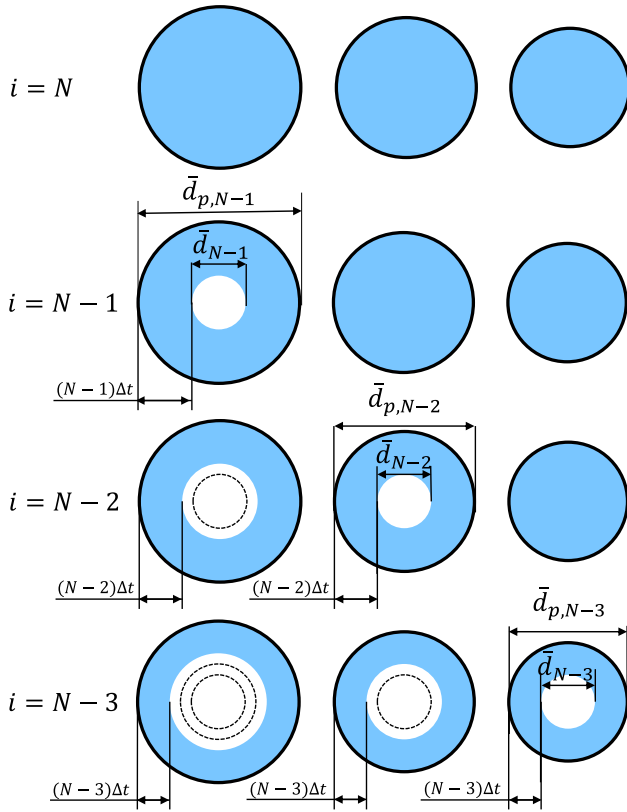
Fig. 3. Schematic representation of the adsorption process and change in "adsorbate" layer thickness between steps $N - 3$ and N (relative dimensions not to scale).

$$V_i^* = V_i - V_{i+1} - \Delta t \sum_{j=i+1}^{N-1} S_{p,j} \left(\frac{\bar{d}_{p,j} - 2\bar{t}_i}{\bar{d}_{p,j}} \right) \tag{12}$$

where $\bar{t}_i = (t_i + t_{i+1})/2 = i\Delta t + \Delta t/2$ is the average "adsorbate" layer thickness between steps i and $i + 1$. Here, V_{i+1} represents the total volume of unfilled space in the pores with diameter larger than $d_{p,i+1}$ when the "adsorbate" layer thickness was t_{i+1}. The third term on the right hand side of Eq. (12) represents the volume of unfilled space created in these pores when the "adsorbate" layer thickness was reduced from t_{i+1} to t_i. Similarly, the corrected surface area S_i^* can be expressed as

$$S_i^* = S_i - \sum_{j=i+1}^{N-1} S_{p,j} \left(\frac{\bar{d}_{p,j} - 2t_i}{\bar{d}_{p,j}} \right). \tag{13}$$

The general expressions for $\bar{d}_i$, $V_{p,i}$, and $S_{p,i}$ assuming cylindrical geometry of the unfilled spaces and pores were

$$\bar{d}_i = 4 \frac{V_i^*}{S_i^*}, \quad \frac{V_{p,i}}{V_i^*} = \left(\frac{\bar{d}_{p,i}}{\bar{d}_i} \right)^2, \quad \text{and} \quad \frac{S_{p,i}}{S_i^*} = \frac{\bar{d}_{p,i}}{\bar{d}_i} \tag{14}$$

where $\bar{d}_{p,i} = (2i + 1)\Delta t$. Note that $V_{p,i}$, and $S_{p,i}$ were constrained to non-negative values.

Then, the cumulative $V_{p,cu}(\bar{d}_{p,i})$ and total $V_{p,tot}$ pore volumes were calculated according to

$$V_{p,cu}(\bar{d}_{p,i}) = \sum_{j=0}^{i} V_{p,j} \quad \text{and} \quad V_{p,tot} = \sum_{j=0}^{N-1} V_{p,j}. \tag{15}$$

The differential pore size distribution was then calculated by interpolating the cumulative pore volume $V_{p,cu}(\bar{d}_{p,i})$ as a function of the average pore diameter $\bar{d}_{p,i}$ with a cubic spline to obtain a continuous function $V_{p,cu}(d_p)$ and its derivative $dV_{p,cu}/dd_p$. Finally, the normalized pore size distribution was calculated by dividing the differential PSD by

Table 1
"Adsorbate" layer thickness Δt, cube size Δx, relative total pore volume error $\delta V_{p,tot}$, specific surface area $A_{g,SC}$, pore diameter range, and average pore diameters $\bar{d}_p$ [Eq. (5)] and $\bar{d}_{p,PSD}$ [Eq. (18)] of the PSDs of surface-contact structures with monodisperse particles of radius $r_s = 2.5$ nm.

	$\phi = 39.6\%$	$\phi = 50.1\%$	$\phi = 60.5\%$	$\phi = 79.1\%$
Δt (nm)	0.1	0.2	0.25	0.5
Δx (nm)	0.10	0.09	0.09	0.09
$\Delta t/\Delta x$	1.0	2.22	2.78	5.55
$\delta V_{p,tot}$	0.90%	2.57%	5.04%	15.20%
$A_{g,SC}$ (m²/g)	330	362	406	479
Pore diameter range (nm)	1.5–9.3	2.2–11.8	2.8–19.3	5.5–27.5
$\bar{d}_p$ (nm)	3.6	5.0	6.9	14.4
$\bar{d}_{p,PSD}$ (nm)	3.8	4.8	6.0	9.5

$V_{p,tot}$ to obtain the probability distribution expressed as

$$f(d_p) = \frac{1}{V_{p,tot}} \frac{dV_{p,cu}}{dd_p}. \tag{16}$$

The PSD calculation algorithm was validated with ideal structures made with one to several pores with cylindrical, cubic, or spherical shapes (see Figs. S2 and S3 in Supporting Information). In addition, the effect of numerical uncertainties on the apparent pore volume V_i and apparent surface area S_i was studied. Random errors within 3% of the exact values of V_i and S_i did not significantly affect the predicted PSDs. This PSD algorithm was applied to the numerically generated structures of particle radius $r_s = 2.5$ nm and porosity ranging from 40 to 80%. Note that when the porosity increased, large pores located at the surface of the simulation domain were more likely to be cut and considered smaller than they really were. Here, numerical convergence also depended on the ratio $\Delta t/\Delta x$ and this ratio was increased with increasing porosity. Table 1 summarizes the increment of the "adsorbate" layer thickness Δt and the discretization cube size Δx used for each porosity. Table 1 also features the relative error $\delta V_{p,tot}$ in calculations of the total pore volume obtained either from porosity calculations or from pore size distribution defined as

$$\delta V_{p,tot} = \frac{\phi L^3 - V_{p,tot}}{\phi L^3}. \tag{17}$$

The relative error $\delta V_{p,tot}$ was less than 6% for porosity $\phi = 39.6$, 50.1, and 60.5%, and reached up to 15.2% for $\phi = 79.1\%$. The relative error $\delta V_{p,tot}$ of the computer-generated structures was comparable to the relative error $\delta V_{p,tot}$ calculated for the ideal structures used for validation. In addition, experimental measurements feature uncertainty within 5%, thus confirming the validity of the algorithm. The relative error was mainly due to the assumption of cylindrical pores which is not satisfied by actual silica aerogels and ambigels nor by computer-generated structures.

Finally, the average diameter $\bar{d}_{p,PSD}$ of the PSDs was calculated from the PSD according to

$$\bar{d}_{p,PSD} = \int_0^\infty d_p f(d_p) dd_p. \tag{18}$$

The results could be compared with the average pore diameter $\bar{d}_{p,PC}$ for point-contact structures with monodisperse particles of radius r_s derived by combining Eqs. (3), (5) and (7) to yield [22]

$$\bar{d}_{p,PC} = \frac{4r_s}{3} \frac{\phi}{1 - \phi}. \tag{19}$$

3.3. Structural characterization - polydisperse nanoparticles

The fraction of overlapping particles and the dimensionless average overlapping distance $\bar{l}_o^*$ were also computed for surface-contact structures with polydisperse nanoparticles. The dimensionless overlapping

distance between two adjacent overlapping particles "j" and "k" in surface-contact structures was defined as $l_o^* = 1 - d_{jk}/(r_{s,j} + r_{s,k})$ where $r_{s,j}$ and $r_{s,k}$ are the radius of the particles and $d_{jk}/(r_{s,j} + r_{s,k})$ is the dimensionless interparticle distance between the particles. The dimensionless average overlapping distance $\bar{l}_o^*$ was then obtained by averaging all computed values of l_o^*. The porosity ϕ of surface-contact structures with polydisperse nanoparticles was calculated using the discretization method detailed previously. Similarly, their specific surface area $A_{g,SC}$ can be calculated in the same manner as for monodisperse structures using Eq. (8). In addition, Eqs. (5) and (7) are still valid for surface-contact structures with polydisperse nanoparticles and can be used to determine A_i and $\bar{d}_p$, respectively.

4. Results and discussion

4.1. Aerogel and ambigel structures

Fig. 4 shows examples of surface-contact structures numerically generated by the DLCCA method consisting of monodisperse particles and featuring porosity ϕ of (a) 50.5, (b) 70.4, and (c) 90.5%. For the three illustrated structures, the final number of clusters was $n_c = 10$, and the total particle number N_s varied from 11,800 to 1549. Fig. 4(d) shows details of a computer-generated high-porosity surface-contact structure with overlapping particles. It resembles the structure of actual silica aerogels observed in the TEM image of Fig. 1(a).

4.2. Structural characterization - monodisperse nanoparticles

4.2.1. Overlapping distance

Fig. 5 shows the dimensionless average overlapping distance $\bar{l}_o^* = 1 - \bar{d}/2r_s$ for surface-contact structures with monodisperse nanoparticles as a function of particle volume fraction f_v for particle radius $r_s = 2.5$, 5, and 10 nm. It indicates that the dimensionless average overlapping distance $\bar{l}_o^*$ increased with particle volume fraction f_v. In other words, the particles overlapped more with decreasing porosity ϕ
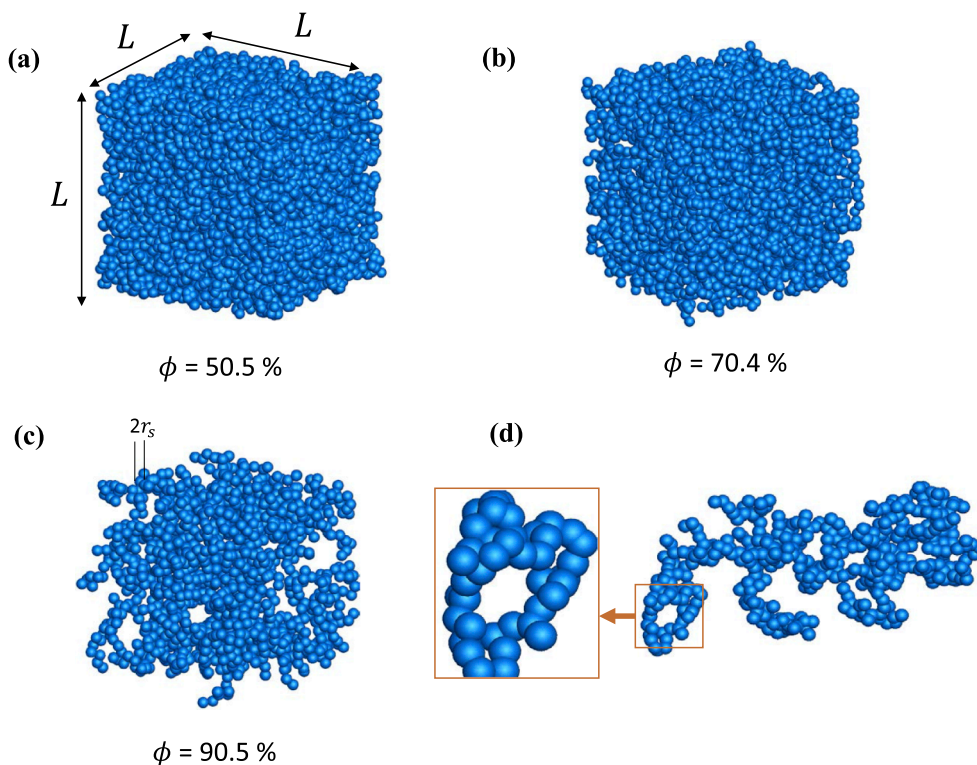
Fig. 5. Computed dimensionless average overlapping distance $\bar{l}_o^* = 1 - \bar{d}/2r_s$ of an aggregate as a function of particle volume fraction f_v and porosity ϕ for $r_s = 2.5$, 5, and 10 nm, along with least-square fit given by Eq. (20).

$= 1 - f_v$. This was consistent with experimental observations for denser aerogels obtained via sintering and featuring lower porosity and larger particle coalescence [14,22,43,48]. It is also interesting to note that the dimensionless average overlapping distance $\bar{l}_o^*$ was independent of the particle radius r_s. Fig. 5 also shows a logarithmic fit ($R^2 = 0.98$) of all data points given by

$$\bar{l}_o^* = 0.076\ln(1 - \phi) + 0.31 \qquad (20)$$

where porosity ϕ varied between 35 and 95%, i.e., particle volume fraction f_v ranged between 5 and 65%. Finally, note that more than 99% of the particles in the nanostructures overlapped with other particles for

Fig. 4. Illustrations of surface-contact structures obtained by DLCCA simulations for (a) $\phi = 50.5\%$, (b) $\phi = 70.4\%$, (c) $\phi = 90.5\%$, and (d) zoom-in of a high-porosity computer-generated surface-contact aerogel structure.
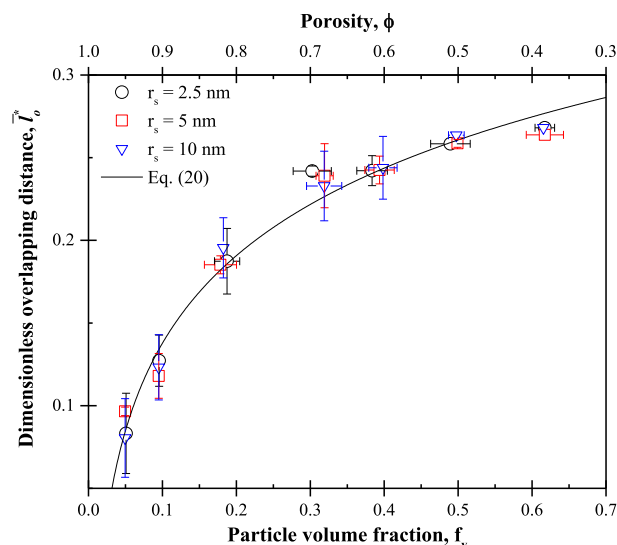
porosity ranging from 60 to 90% and for all values of radius r_s considered.

4.2.2. Specific surface area and interfacial area concentration

Fig. 6 shows (a) the specific surface area A_g and (b) the interfacial area concentration A_i as functions of porosity ϕ computed for both point-contact and surface-contact aerogel structures consisting of monodisperse particles. It indicates that the specific surface area $A_{g,PC}$ for point-contact structures computed using Eq. (8) was in excellent agreement with the theoretical predictions of Eq. (7). Consequently, good agreement was also observed for $A_{i,PC} = A_{g,PC}\rho_s(1-\phi)$. The specific surface area $A_{g,PC}$ depended only on the particle radius r_s and was independent of porosity ϕ. On the other hand, the interfacial area concentration $A_{i,PC}$ was linearly proportional to porosity ϕ and decreased with increasing particle radius r_s.

Moreover, for surface-contact structures, the specific surface area $A_{g,SC}$ [Eq. (8)] was systematically lower than that of point-contact structures $A_{g,PC}$ for a given particle radius r_s. Furthermore, $A_{g,SC}$ increased with increasing porosity ϕ, i.e., with decreasing dimensionless average overlapping distance $\bar{l}_o^*$. This suggests that surface-contact structures with higher particle overlap (or coalescence) had lower specific surface area, in agreement with previous studies [15]. Indeed, Iler [15] reported that the theoretical specific surface area $A_{g,PC}$ [Eq. (7)] was greater than the experimentally measured specific surface area $A_{g,BET}$ of silica aerogels in which the particles were "cemented together". The author detailed that the ratio of the theoretical point-contact and experimental BET specific surface areas $A_{g,PC}/A_{g,BET}$ was greater than 1.1 for silica aerogels featuring strong coalescence between the particles [15]. This ratio was used as an indication of the interparticle overlapping. In the present study, the ratio of the theoretical point-contact to the computed surface-contact specific surface area $A_{g,PC}/A_{g,SC}$, varied from 1.05 to 1.77 as the porosity ϕ decreased from 95 to 40% and the dimensionless average overlapping distance $\bar{l}_o^*$ increased from 0.05 to 0.27. The specific surface areas $A_{g,SC}$ and $A_{g,PC}$ were found to be related by the following simple ad hoc expression

$$A_{g,SC}(r_s, \phi) = [(1 - \bar{l}_o^*)(\phi - 1) + 1]A_{g,PC}(r_s) \quad (21)$$

where $\bar{l}_o^*(\phi)$ was predicted by Eq. (20). Eq. (21) was derived to satisfy the following observations: (i) the upper bound of $A_{g,SC}$ as ϕ tended to 100% was $A_{g,PC}$, (ii) overlapping reduced the specific surface area, and (iii) $A_{g,SC}$ increases linearly with porosity ϕ. Fig. 6(a) indicates that predictions by Eq. (21) combined with Eq. (7) for $A_{g,PC}$ and Eq. (20) for $\bar{l}_o^*$ agreed well with numerical results.

Finally, Fig. 6 shows measurements of $A_{g,BET}$ reported in the literature [45,46] for silica aerogels and ambigels with porosity ϕ between 76 ± 5 and $92 \pm 5\%$ and particle radius r_s between 1.4 ± 0.05 and 3 ± 0.05 nm. The measured specific surface area $A_{g,BET}$ fell between $A_{g,SC}$ and $A_{g,PC}$. In fact, it was systematically smaller than or equal to the theoretical specific surface area $A_{g,PC}$ for a given particle radius r_s. Therefore, the experimental data was consistent with the fact that $A_{g,PC}(r_s)$ corresponds to the maximum specific surface area for a structure with dense particles of radius r_s, as previously discussed.

Fig. 7 shows the computed specific surface areas $A_{g,PC}$ and $A_{g,SC}$ as functions of particle radius r_s for point-contact structures and surface-contact structures with monodisperse nanoparticles and porosity $\phi = 40\%$. It also shows predictions of (i) $A_{g,PC}$ by Eq. (7) for point-contact structures and (ii) $A_{g,SC}$ by Eq. (21) for surface-contact structures corresponding to $\phi = 40\%$ and a dimensionless average overlapping distance $\bar{l}_o^* = 0.27$ (Fig. 5). First, Fig. 7 indicates that the specific surface area $A_{g,PC}$ decreased with increasing particle radius r_s and was in excellent agreement with predictions by Eq. (7), as previously mentioned. Similarly, the specific surface area $A_{g,SC}$ of surface-contact structures decreased with decreasing r_s and differed by less than 3% with predictions by Eq. (21). Fig. 7 also features experimental data $A_{g,BET}$ reported in the literature for silica aerogels [46] and ambigels [45,47]. It is

interesting to note that, here also, experimental data for $A_{g,BET}$ fell between predictions for point-contact structures $A_{g,PC}$ and computational results for surface-contact structures $A_{g,SC}$.

Fig. 8 plots the specific surface area A_g as a function of porosity ϕ measured experimentally for sintered silica aerogels [43] and computed for surface-contact structures $A_{g,SC}$ [Eq. (21)] with an overlapping distance l_o^* estimated using Eq. (20). It indicates that $A_{g,SC}$ increased with increasing porosity ϕ. These results were consistent with other experimental data for sintered silica ambigels and aerogels [49,50]. Moreover, predictions by Eq. (21) were in very good agreement with experimental measurements for $\phi < 80\%$. However, for $\phi > 80\%$, discrepancies were apparent and likely due to the reported average particle radius which corresponded to that of the "secondary particles", i.e., the particles resulting from the agglomeration of primary particles [51]. For larger porosities, such secondary particles were porous and micropores contributed to the surface area [51]. However, these micropores were ignored in the simulations and collapsed during the sintering process as the porosity decreased [43].

Overall, the measured specific surface area $A_{g,BET}$ of aerogels can be used to provide information on the primary particle radius r_s and interparticle coalescence. Indeed, the specific surface area of point-contact structures $A_{g,PC}(r_s)$ represents the maximum specific surface area for structures with monodisperse particle of radius r_s. Thus, an upper
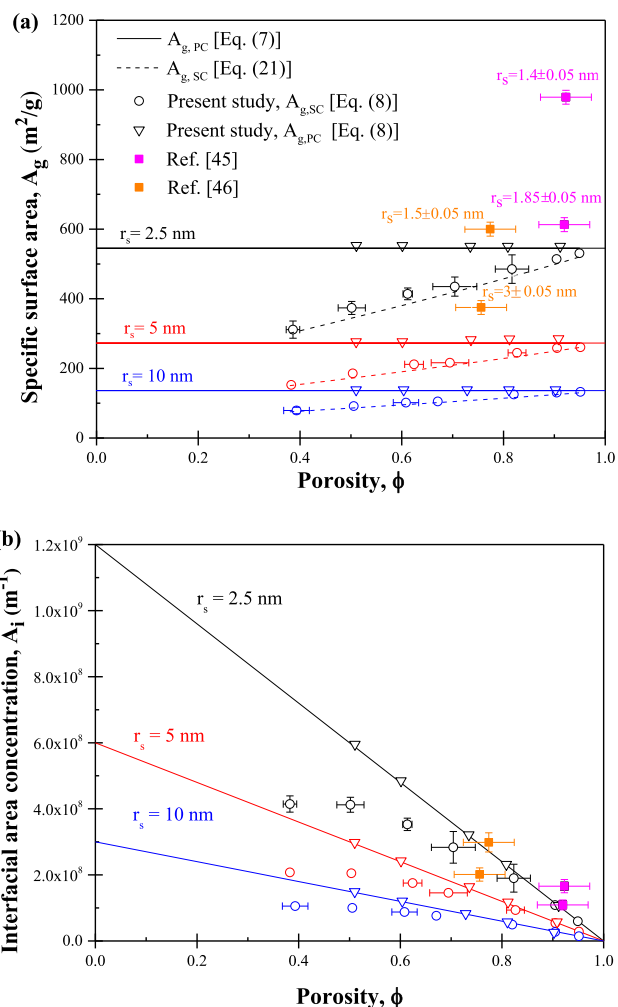

Fig. 6. Computed (a) specific surface area A_g (in m^2/g) and (b) interfacial area concentration A_i (in m^{-1}) of point-contact and surface-contact structures as functions of porosity ϕ for monodisperse spheres of radius $r_s = 2.5$, 5, and 10 nm, along with predictions by Eqs. (7) and (21), and experimental data from Refs. [45,46].
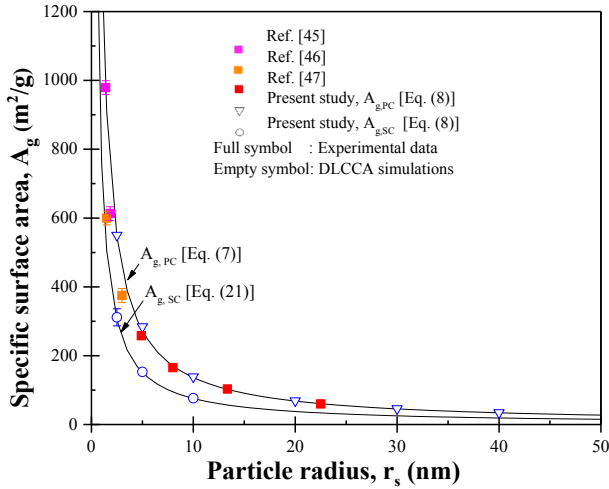
Fig. 7. Computed specific surface area A_g (in m^2/g) of point-contact and surface-contact structures with monodisperse nanoparticles as a function of particle radius r_s, along with predictions by Eqs. (7) and (21) with $\bar{l}_o^* = 0.27$ for $\phi = 40\%$, as well as experimental data from Refs. [45–47].
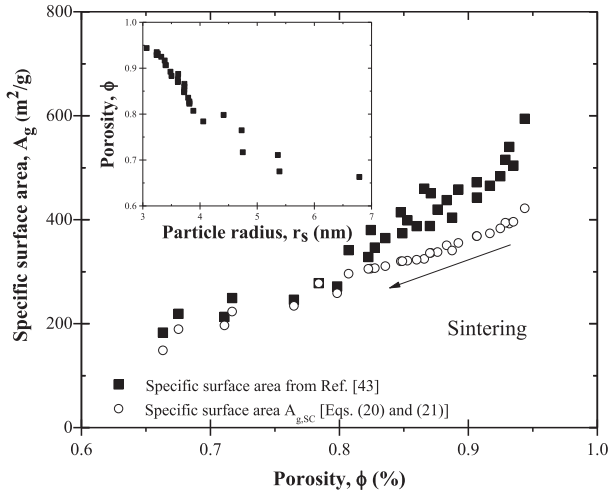

Fig. 8. Comparison between the specific surface area A_g of sintered silica aerogels from Ref. [43] and the specific surface area $A_{g,SC}$ calculated from Eqs. (20) and (21) for aerogels with monodisperse overlapping spherical particles as functions of porosity ϕ. Inset: porosity ϕ of the sintered silica aerogels from Ref. [43] as a function of average particle radius r_s.

limit of the silica aerogel's particle radius can be determined from the measured $A_{g,BET}$ based on Eq. (7). In addition, a more precise estimate of the particle radius could be determined if the average overlapping distance $\bar{l}_o^*$ of the aggregate was also known. The latter could be inferred from Eq. (20) and porosity measurement. Finally, the specific surface area is also an indication of the interparticle coalescence such that a ratio $A_{g,PC}/A_{g,BET} \sim 1$ indicates little coalescence (i.e., overlapping) while a ratio $A_{g,PC}/A_{g,BET} > 1.1$ indicates strong coalescence between the particles [15].

4.2.3. Pore size distributions

Fig. 9 shows (a) the normalized cumulative pore volume $V_{p,cu}/V_{p,tot}$ and (b) the differential pore size distribution $f(d_p)$, obtained by the algorithm previously described, for computer-generated surface-contact structures with monodisperse particles of radius $r_s = 2.5$ nm and porosity ϕ ranging from 40 to 80%. Table 1 summarizes the range of pore size and the average pore diameter $\bar{d}_{p,PSD}$ obtained from the differential PSDs [Eq. (18)] with porosity ϕ between 40 and 80%. Fig. 9 indicates that the structures with lower porosity ϕ featured smaller pores and

narrower pore size distribution. For example, Table 1 indicates that the pore diameter d_p ranged (i) from 1.5 to 9.3 nm for porosity $\phi = 39.6\%$, and (ii) from 5.5 to 27.5 nm for porosity $\phi = 79.1\%$. In addition, Fig. 9(a) plots experimental PSDs for silica ambigels and aerogel with porosity $\phi = 41$, 42, 54, and 80% reported by Harreld et al. [44]. It indicates that the numerically predicted PSDs were in good agreement with experimental measurements. Note that the particle radius r_s of the synthesized mesoporous silica was not reported [44]. However, the measured specific surface area $A_{g,BET}$ for the four silica ambigels and aerogels considered was larger than $A_{g,PC}(r_s = 5$ nm) predicted by Eq. (7), indicating that, experimentally, the silica nanoparticles were smaller than 5 nm.

Table 1 shows that the average pore diameter $\bar{d}_{p,PSD}$ of computer-generated structures ranged from 3.8 to 9.5 nm for porosity ϕ ranging from 39.6 to 79.1%. These results were also in good agreement with experimental measurements for silica ambigels and aerogels with porosity between 41 and 80% reported in Ref. [44].

4.2.4. Average pore diameter

Fig. 10 shows the average pore diameter $\bar{d}_p$, estimated by Eq. (5), (a) as a function of the particle radius r_s for $\phi = 50$ and 80%, and (b) as a function of porosity ϕ for $r_s = 2.5$, 5, and 10 nm for computer-generated
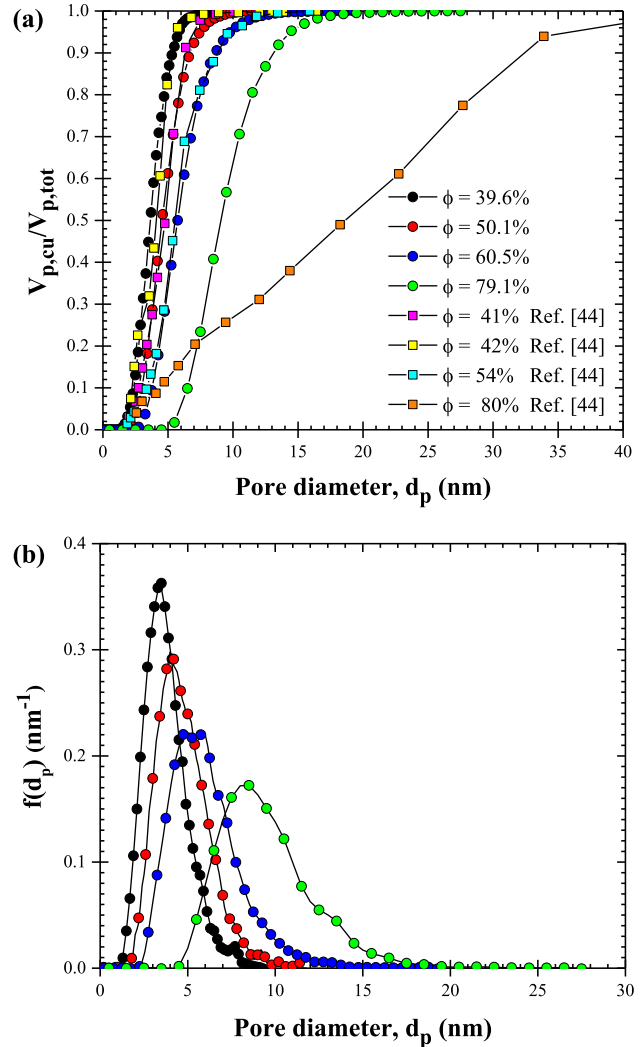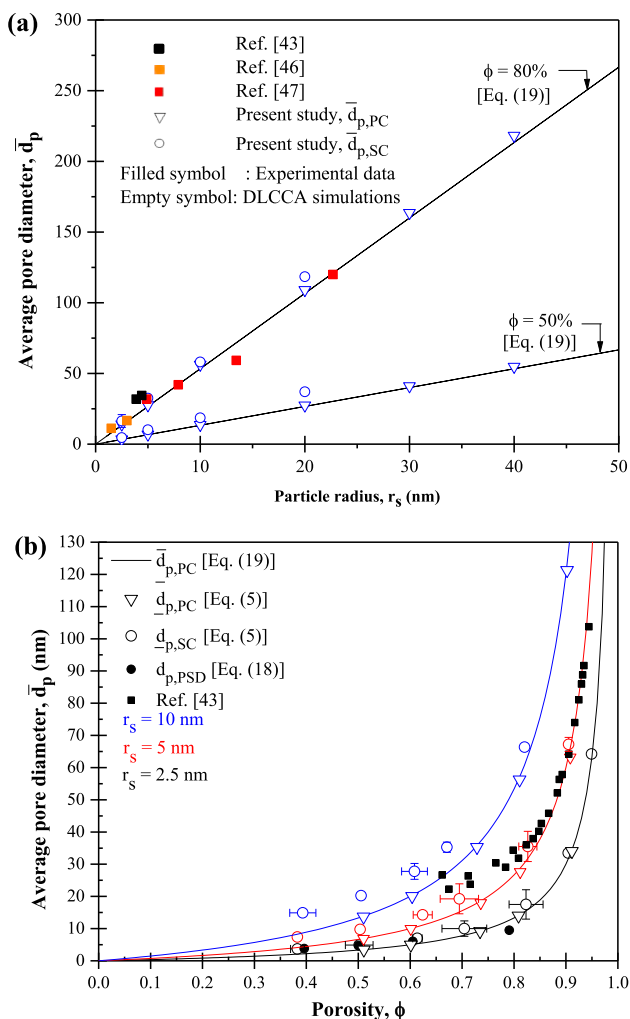

Fig. 9. (a) Normalized cumulative pore volume $V_{p,cu}/V_{p,tot}$ and (b) differential PSDs $f(d_p)$ of computer-generated surface-contact structures with monodisperse particle radius $r_s = 2.5$ nm and porosity ranging from 39.6 to 89.1% along with experimental measurements from Ref. [44].
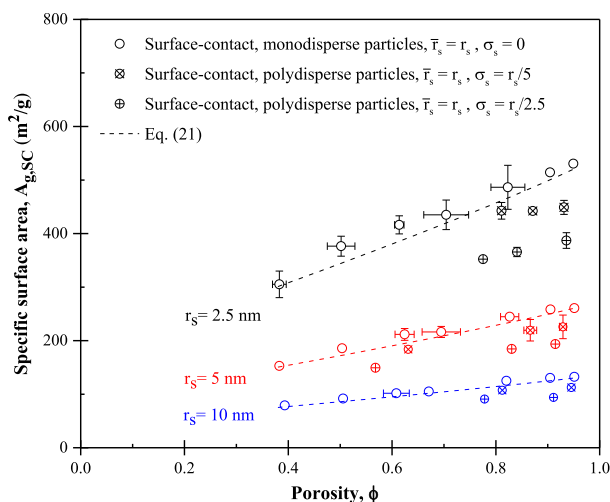
Fig. 11. Specific surface area $A_{g,SC}$ as a function of porosity ϕ for surface-contact structures of polydisperse nanoparticles of mean radius $\bar{r}_s$ and standard deviation σ_s. Results for the specific surface area of surface-contact structures with monodisperse particles are also shown for reference.

from 39.6 to 79.1%.

4.3. Effect of particle polydispersity

Fig. 11 shows the specific surface area of surface-contact structures $A_{g,SC}$ consisting of polydisperse particles following a Gaussian distribution with three values of mean radius $\bar{r}_s$ = 2.5, 5, and 10 nm and three values of standard deviation σ_s = 0 (monodisperse), $r_s/5$, and $r_s/2.5$. It indicates that the specific surface area of surface-contact structures consisting of polydisperse particles was lower than that of monodisperse particles with the same mean radius. In addition, for a given mean radius $\bar{r}_s$, larger standard deviation σ_s resulted in smaller specific surface area. Note, however, that a smaller fraction of particles overlapped in structures with polydisperse particles (75–95%) than in structures with monodisperse particles (99%). Finally, polydispersity of the constitutive particles resulted also in lower interfacial area concentration A_i [Eq. (7)] and larger average pore diameter $\bar{d}_p$ [Eq. (5)] for both point-contact and surface-contact structures.

5. Conclusion

This study aimed to numerically generate mesoporous structures and assess the effects of porosity, particle radius, polydispersity, and overlapping on the structural characteristics of mesoporous materials. Point-contact and surface-contact structures with either monodisperse or polydisperse particles were generated numerically using the DLCCA method. Porosity was varied from 35 to 95% and particle radius from 2.5 to 40 nm. The computer-generated mesoporous materials were characterized numerically in terms of specific surface area, average pore diameter, and pore size distribution in complete analogy with experimental characterization. In particular, a new algorithm, inspired by gas adsorption porosimetry, was developed to compute the specific surface area and pore size distribution of computer-generated structures. The specific surface area for point-contact structures corresponded to the maximum specific surface area of mesoporous material for a given primary particle radius. For given porosity and particle radius, particles overlapping and/or polydispersity reduced the specific surface area and interfacial concentration but increased the average pore diameter. Finally, the structural properties of the computer-generated structures agree well with those reported for silica aerogel and ambigel. The computational tools and methods can be used in the discovery and optimization of mesoporous materials (e.g., silica, carbon

---

Fig. 10. Computed average pore diameter $\bar{d}_p$ (in nm) [Eqs. (5) and (18)] of point-contact and surface-contact mesoporous structures consisting of monodisperse spheres of radius r_s as a function of (a) particle radius r_s between 2.5 and 40 nm for ϕ = 50 or 80% and (b) porosity ϕ for r_s = 2.5, 5, and 10 nm. Predictions of $\bar{d}_{p,PC}$ [Eq. (19)] are also shown, as well as experimental data from Refs. [43,46,47].

point-contact and surface-contact structures consisting of monodisperse spheres. It also plots predictions of $\bar{d}_{p,PC}$ by Eq. (19) and experimental data for silica aerogels reported in the literature for silica aerogels with porosity ϕ around 80% [43,45,47]. First, Fig. 10 indicates that both $\bar{d}_{p,PC}$ and $\bar{d}_{p,SC}$ (i) increased linearly with increasing particle radius r_s and (ii) increased sharply with increasing porosity ϕ. It also shows that the average pore diameter of surface-contact structures $\bar{d}_{p,SC}$ was slightly larger than predictions of $\bar{d}_{p,PC}$ for point-contact structures [Eq. (19)]. The difference between $\bar{d}_{p,PC}$ and $\bar{d}_{p,SC}$ increased with decreasing porosity ϕ due to the larger associated particle overlapping.

Moreover, Fig. 10(a) shows that the average pore diameters reported in the literature [43,45,47] were in good agreement with (i) numerical simulations and (ii) predictions of $\bar{d}_{p,PC}$ by Eq. (19). Moreover, Fig. 10(b) plots the average pore diameter $\bar{d}_p$ reported for sintered silica aerogels with different porosities [43]. It indicates that the sharp increase in $\bar{d}_p$ with increasing porosity ϕ was also observed experimentally for sintered silica aerogels.

Finally, Fig. 10(b) plots the average diameter $\bar{d}_{p,PSD}$ obtained from the differential PSDs [Eq. (18)] of surface-contact structures consisting of monodisperse nanoparticles. It shows that the average diameter $\bar{d}_{p,PSD}$ was in good agreement with the average pore diameter of surface-contact structures $\bar{d}_{p,SC}$ computed using Eq. (5) for porosity ϕ ranging

[4], or alumina [5], or ceria [6]) and to relate their nanoscale architecture to their mechanical, optical, and thermal properties.

Data availability

The processed data required to reproduce these findings are available upon request.

CRediT authorship contribution statement

Tiphaine Galy: Conceptualization, Formal analysis, Data curation, Visualization, Writing - original draft. **Du Mu:** Conceptualization, Formal analysis, Data curation, Visualization. **Michal Marszewski:** Methodology, Writing - original draft. **Laurent Pilon:** Conceptualization, Methodology, Project administration, Supervision, Writing - review & editing.

Acknowledgment

Appendix A. Supplementary material

The Supporting Information is available free of charge on https://pubs.acs.org/. Illustration of two overlapping spheres and of the cube discretization method (Fig. S1). Table with theoretical and computed porosity, surface area, and specific surface area of two overlapping spheres (Table S1). Differential pore size distributions of structures with cylindrical, spherical or cubic pores (Figs. S2 and S3). Tables with "adsorbate" layer thickness and error on the total pore volume for structures with cylindrical, spherical, or cubic pores (Tables S2 and S3). Supplementary data associated with this article can be found, in the online version, at https://doi.org/10.1016/j.commatsci.2018.10.035.

References

[1] M. Thommes, K. Kaneko, A. Neimark, J. Olivier, F. Rodriguez-Reinoso, J. Rouquerol, K. Sing, Physisorption of gases, with special reference to the evaluation of surface area and pore size distribution (IUPAC technical report), Pure Appl. Chem. 87 (9-10) (2015) 1051–1069, https://doi.org/10.1515/pac-2014-1117.

[2] A. Dorcheh, M. Abbasi, Silica aerogel; synthesis, properties and characterization, J. Mater. Proces. Technol. 199 (1) (2008) 10–26, https://doi.org/10.1016/j.jmatprotec.2007.10.060.

[3] E. Cuce, P. Cuce, C. Wood, S. Riffat, Toward aerogel based thermal superinsulation in buildings: a comprehensive review, Renew. Sustain. Energy Rev. 34 (2014) 273–299, https://doi.org/10.1016/j.rser.2014.03.017.

[4] C. Moreno-Castilla, F. Maldonado-Hódar, Carbon aerogels for catalysis applications: An overview, Carbon 43 (3) (2005) 455–465, https://doi.org/10.1016/j.carbon.2004.10.022.

[5] G. Zu, J. Shen, L. Zou, W. Wang, Y. Lian, Z. Zhang, A. Du, Nanoengineering super heat-resistant, strong alumina aerogels, Chem. Mater. 25 (23) (2013) 4757–4764, https://doi.org/10.1021/cm402900y.

[6] C. Laberty-Robert, J. Long, E. Lucas, K. Pettigrew, R. Stroud, M. Doescher, D. Rolison, Sol-gel-derived ceria nanoarchitectures: synthesis, characterization, and electrical properties, Chem. Mater. 18 (1) (2006) 50–58, https://doi.org/10.1021/cm051385t.

[7] T. Coquil, E. Richman, N. Hutchinson, S. Tolbert, L. Pilon, Thermal conductivity of cubic and hexagonal mesoporous silica thin films, J. Appl. Phys. 106 (3) (2009) 034910, https://doi.org/10.1063/1.3182826.

[8] T. Woignier, J. Reynes, J. Phalippou, J. Dussossoy, Nuclear waste storage in gel-derived materials, J. Sol-Gel. Sci. Technol. 19 (1) (2000) 833–837, https://doi.org/10.1023/A:1008784822052.

[9] G. Kim, S. Hyun, H. Park, Synthesis of low-dielectric silica aerogel films by ambient

[10] R. Baetens, B.P. Jelle, A. Gustavsen, Aerogel insulation for building applications: a state-of-the-art review, Energy Build. 43 (4) (2011) 761–769, https://doi.org/10.1016/j.enbuild.2010.12.012.

[11] H. Maleki, L. Durães, A. Portugal, Synthesis of lightweight polymer-reinforced silica aerogels with improved mechanical and thermal insulation properties for space applications, Microporous Mesoporous Mater. 197 (2014) 116–129, https://doi.org/10.1016/j.micromeso.2014.06.003.

[12] E. Holt, The properties and forming of catalysts and absorbents by granulation, Powder Technol. 140 (3) (2004) 194–202, https://doi.org/10.1016/j.powtec.2004.01.010.

[13] F. Klenert, J. Fruhstorfer, C. Aneziris, U. Gross, D. Trimis, I. Reichenbach, D. Vijay, A. Horn, Microstructure and transmittance of silica gels for application as transparent heat insulation materials, J. Sol-Gel. Sci. Technol. 75 (3) (2015) 602–616, https://doi.org/10.1007/s10971-015-3731-3.

[14] T. Woignier, J. Reynes, A.H. Alaoui, I. Beurroies, J. Phalippou, Different kinds of structure in aerogels: relationships with the mechanical properties, J. Non-Cryst. Solids 241 (1) (1998) 45–52, https://doi.org/10.1016/S0022-3093(98)00747-9.

[15] R. Iler, The Colloid Chemistry of Silica and Silicates Vol. 80 Cornell University Press, Ithaca, NY, 1955.

[16] J. Primera, A. Hasmy, T. Woignier, Numerical study of pore sizes distribution in gels, J. Sol-Gel. Sci. Technol. 26 (1) (2003) 671–675, https://doi.org/10.1023/A:1020765230983.

[17] J. Primera, T. Woignier, A. Hasmy, Pore structure simulation of gels with a binary monomer size distribution, J. Sol-Gel. Sci. Technol. 34 (3) (2005) 273–280, https://doi.org/10.1007/s10971-005-2524-5.

[18] V. Morales-Flórez, N. De La Rosa-Fox, M. Pinero, L. Esquivias, The cluster model: a simulation of the aerogel structure as a hierarchically-ordered arrangement of randomly packed spheres, J. Sol-Gel Sci. Technol. 35 (3) (2005) 203–210, https://doi.org/10.1007/s10971-005-2363-4.

[19] V. Morales-Flórez, M. Pinero, N. De La Rosa-Fox, L. Esquivias, J. Anta, J. Primera, The cluster model: A hierarchically-ordered assemblage of random-packing spheres for modelling microstructure of porous materials, J. Non-Cryst. Solids 354 (2) (2008) 193–198, https://doi.org/10.1016/j.jnoncrysol.2007.07.061.

[20] H. Ma, X. Zheng, X. Luo, Y. Yi, F. Yang, Simulation and analysis of mechanical properties of silica aerogels: From rationalization to prediction, Materials 11 (2) (2018) 214, https://doi.org/10.3390/ma11020214.

[21] H.-S. Ma, A.P. Roberts, J.-H. Prévost, R. Jullien, G.W. Scherer, Mechanical structure-property relationship of aerogels, J. Non-Cryst. Solids 277 (2-3) (2000) 127–141, https://doi.org/10.1016/S0022-3093(00)00288-X.

[22] C. Brinker, G. Scherer, Sol-Gel Science, Academic Press, London, UK, 2013.

[23] R. Iler, The Chemistry of Silica, John Wiley & Sons, Chichester, UK, 1979.

[24] D. Rolison, B. Dunn, Electrically conductive oxide aerogels: new materials in electrochemistry, J. Mater. Chem. 11 (4) (2001) 963–980, https://doi.org/10.1039/B007591O.

[25] J. Long, K. Swider-Lyons, R. Stroud, D. Rolison, Design of pore and matter architectures in manganese oxide charge-storage materials, Electrochem. Solid-State Lett. 3 (10) (2000) 453–456, https://doi.org/10.1149/1.1391177.

[26] H. Ma, E. Ding, W. Wang, Power reduction with enhanced sensitivity for pellistor methane sensor by improved thermal insulation packaging, Sensors Actuat. B: Chem. 187 (2013) 221–226, https://doi.org/10.1016/j.snb.2012.10.121.

[27] S.-W. Hwang, H.-H. Jung, S.-H. Hyun, Y.-S. Ahn, Effective preparation of crack-free silica aerogels via ambient drying, J. Sol-Gel. Sci. Technol. 41 (2) (2007) 139–146, https://doi.org/10.1007/s10971-006-0513-y.

[28] D. Schaefer, Polymers, fractals and ceramic materials, Science 243 (4894) (1989) 1023–1027, https://doi.org/10.1126/science.243.4894.1023.

[29] J. Martin, D. Adolf, The sol-gel transition in chemical gels, Annu. Rev. Phys. Chem. 42 (1) (1991) 311–339, https://doi.org/10.1146/annurev.pc.42.100191.001523.

[30] P. Meakin, T. Vicsek, F. Family, Dynamic cluster-size distribution in cluster-cluster aggregation: Effects of cluster diffusivity, Phys. Rev. B 31 (1) (1985) 564, https://doi.org/10.1103/PhysRevB.31.564.

[31] A. Hasmy, M. Foret, E. Anglaret, J. Pelous, R. Vacher, R. Jullien, Small-angle neutron scattering of aerogels: simulations and experiments, J. Non-Crystall. Solids 186 (1995) 118–130, https://doi.org/10.1016/0022-3093(95)00046-1.

[32] S. Lallich, F. Enguehard, D. Baillis, Experimental determination and modeling of the radiative properties of silica nanoporous matrices, ASME J. Heat Transfer 131 (8) (2009) 082701, https://doi.org/10.1115/1.3109999.

[33] J.-J. Zhao, Y.-Y. Duan, X.-D. Wang, B.-X. Wang, A 3-D numerical heat transfer model for silica aerogels based on the porous secondary nanoparticle aggregate structure, J. Non-Cryst. Solids 358 (10) (2012) 1287–1297, https://doi.org/10.1016/j.jnoncrysol.2012.02.035.

[34] L. Gelb, K. Gubbins, Pore size distributions in porous glasses: a computer simulation study, Langmuir 15 (2) (1999) 305–308, https://doi.org/10.1021/la9808418.

[35] S. Gavalda, K. Gubbins, Y. Hanzawa, K. Kaneko, K. Thomson, Nitrogen adsorption in carbon aerogels: A molecular simulation study, Langmuir 18 (6) (2002) 2141–2151, https://doi.org/10.1021/la011132o.

[36] J.-C. Cuillière, An adaptive method for the automatic triangulation of 3D parametric surfaces, Comput.-Aided Des. 30 (2) (1998) 139–149, https://doi.org/10.1016/S0010-4485(97)00085-7.

[37] M. Thommes, Physical adsorption characterization of ordered and amorphous mesoporous materials, Nanoporous Mater.: Sci. Eng. 11 (2004) 317–364, https://doi.org/10.1142/9781860946561_0011.

[38] S. Brunauer, P. Emmett, E. Teller, Adsorption of gases in multimolecular layers, J. Am. Chem. Soc. 60 (2) (1938) 309–319, https://doi.org/10.1021/ja01269a023.

[39] E. Barrett, L. Joyner, P. Halenda, The determination of pore volume and area

distributions in porous substances. I. computations from nitrogen isotherms, J. Am. Chem. Soc. 73 (1) (1951) 373–380, https://doi.org/10.1021/ja01145a126.

[40] L. Skinner, J. Sambles, The kelvin equation: a review, J. Aerosol Sci. 3 (3) (1972) 199–210, https://doi.org/10.1016/0021-8502(72)90158-9.

[41] M. Jaroniec, M. Kruk, J. Olivier, Standard nitrogen adsorption data for characterization of nanoporous silicas, Langmuir 15 (16) (1999) 5410–5413, https://doi.org/10.1021/la990136e.

[42] G. Scherer, Effect of drying on properties of silica gel, J. Non-Cryst. Solids 215 (2-3) (1997) 155–168, https://doi.org/10.1016/S0022-3093(97)00079-3.

[43] A. Emmerling, J. Gross, R. Gerlach, R. Goswin, G. Reichenauer, J. Fricke, H.-G. Haubold, Isothermal sintering of SiO_2 aerogels, J. Non-Cryst. Solids 125 (3) (1990) 230–243, https://doi.org/10.1016/0022-3093(90)90853-E.

[44] J. Harreld, T. Ebina, N. Tsubo, G. Stucky, Manipulation of pore size distributions in silica and ormosil gels dried under ambient pressure conditions, J. Non-Cryst. Solids 298 (2) (2002) 241–251, https://doi.org/10.1016/S0022-3093(01)01051-1.

[45] M.-A. Einarsrud, E. Nilsen, Strengthening of water glass and colloidal sol based silica gels by aging in TEOS, J. Non-Cryst. Solids 226 (1) (1998) 122–128, https://doi.org/10.1016/S0022-3093(98)00370-6.

[46] M.-A. Einarsrud, E. Nilsen, A. Rigacci, G.M. Pajonk, S. Buathier, D. Valette, M. Durant, B. Chevalier, P. Nitz, F. Ehrburger-Dolle, Strengthening of silica gels and aerogels by washing and aging processes, J. Non-Cryst. Solids 285 (1) (2001) 1–7, https://doi.org/10.1016/S0022-3093(01)00423-9.

[47] J. Ramsey, Sol-Gel Processing, Butterworth, Oxford, UK, 1994.

[48] G. Scherer, S. Calas, R. Sempéré, Sintering aerogels, J. Sol-Gel Sci. Technol. 13 (1-3) (1998) 937–943, https://doi.org/10.1023/A:1008687610326.

[49] G. Scherer, S. Calas, R. Sempéré, Densification kinetics and structural evolution during sintering of silica aerogel, J. Non-Cryst. Solids 240 (1-3) (1998) 118–130, https://doi.org/10.1016/S0022-3093(98)00696-6.

[50] S. Haereid, M. Dahle, S. Lima, M.-A. Einarsrud, Preparation and properties of monolithic silica xerogels from TEOS-based alcogels aged in silane solutions, J. Non-Cryst. Solids 186 (1995) 96–103, https://doi.org/10.1016/0022-3093(95)00039-9.

[51] J. Fricke, SiO_2 aerogels: modifications and applications, J. Non-Cryst. Solids 121 (1-3) (1990) 188–192, https://doi.org/10.1016/0022-3093(90)90129-A.